

**Effective 3D failure simulations by combining
the advantages of embedded strong
discontinuity approaches and classical
interface elements**

R. Radulović & J. Mosler

This is a preprint of an article accepted by:
Engineering Fracture Mechanics (2011)

Effective 3D failure simulations by combining the advantages of embedded strong discontinuity approaches and classical interface elements

R. Radulović & J. Mosler

Materials Mechanics

Institute for Materials Research
Helmholtz-Zentrum Geesthacht
D-21502 Geesthacht, Germany
E-Mail: joern.mosler@hzg.de

Abstract

An efficient numerical framework suitable for three-dimensional analyses of brittle material failure is presented. The proposed model is based on an (embedded) Strong Discontinuity Approach (SDA). Hence, the deformation mapping is elementwise additively decomposed into a conforming, continuous part and an enhanced part associated with the kinematics induced by material failure. To overcome locking effects and to provide a continuous crack path approximation, the approach is extended and combined with advantages known from classical interface elements. More precisely, several discontinuities each of them being parallel to a facet of the respective finite element are considered. By doing so, crack path continuity is automatically fulfilled and no tracking algorithm is necessary. However, though this idea is similar to that of interface elements, the novel SDA is strictly local (finite element level) and thus, it does not require any modification of the global data structure, e.g., no duplication of nodes. An additional positive feature of the advocated finite element formulation is that it leads to a symmetric tangent matrix. It is shown that several simultaneously active discontinuities in each finite element are required to capture highly localized material failure. The performance and predictive ability of the model are demonstrated by means of two benchmark examples.

1 Introduction

Failure of engineering materials and structures is a result of a complex interplay between different physical phenomena such as void nucleation, micro-cracking and other irreversible processes. These micro-defects merge eventually into one or more macro-cracks leading to a reduction of the load-carrying capacity and finally, to failure of the considered structure. During the last few decades, different computational approaches have been developed for the description of such phenomena.

For the numerical modeling of material failure, two different frameworks can be applied in general: smeared crack and discrete crack approaches. Smeared crack approaches fall into the range of continuum mechanics, i.e., they are based on a continuous approximation of the deformation mapping. The kinematics associated with cracks is taken into account by a respective strain field, while stress-softening is captured by a stiffness degradation and a reduction of the strength in the considered material point. It is well known that

a straightforward implementation of such models into a finite element formulation leads to pathological mesh-dependent results, cf. de Borst (2001). Therefore, a regularization of these ill-posed problems by means of different strategies such as higher-order gradient terms or nonlocal theories is required, cf. Peerlings et al. (1998); Pijaudier-Cabot & Bazant (1987). Though the resulting regularized smeared crack approaches are mesh-objective, the associated numerical costs are relatively high. More precisely, three to five finite elements across the thickness of the failure zone are usually required for capturing the localized deformation sufficiently. In large scale structural computations the required computational costs may be prohibitive, even if adaptive techniques are used.

By way of contrast, a crack (fracture process zone) is geometrically represented as a surface having a zero thickness within discrete crack approaches. The kinematics of a crack is described by a displacement discontinuity (crack opening width) and material degradation is captured by a so-called *cohesive law*. Such laws trace back to Dugdale (1960) for ductile materials and Barenblatt (1962) for brittle materials. Within these models, it is assumed that cohesive tractions (stress vector acting at the crack), usually given in terms of the crack width (displacement discontinuity), resist to the separation of the bulk material through the crack. Consequently, discrete crack approaches are based on traction-separation laws (instead of a classical stress-strain-relationship). In contrast to classical stress-strain-based constitutive models, the fracture energy predicted by traction-separation laws does not depend on the size of the respective finite elements yielding physically objective results. Hence, sophisticated regularization techniques such as those mentioned before are not necessary. An additional advantage of the discrete crack approaches is that the width of the crack is zero (with respect to the undeformed configuration) independent of the considered finite element triangulation. Consequently, the length scales associated with material failure and that of the macroscopic structure are, by definition, uncoupled. As a result, discrete crack approaches naturally account for the multi-scale character of material failure. From this follows that relatively large finite elements compared to the width of the localization zone can be used. Hence, such methods are best suited for large scale structural applications.

In the frame of discrete crack approaches, different concepts have been developed for modeling the kinematics of cracks. One possible classification of these concepts is by the location of the displacement discontinuities:

- interface elements - the crack is inserted between standard bulk finite elements (cf. Goodman et al. (1968); Needleman (1990); Ortiz & Pandolfi (1999))
- the crack is embedded into existing bulk finite elements (cf. Belytschko & Black (1999); Dvorkin et al. (1990); Hansbo & Hansbo (2002)).

In the following, each of these kinematical descriptions of cracks, independently of the respective material model, is concisely analyzed and the respective advantages are highlighted.

The first kinematical description of cracks discussed here are interface elements, cf. Goodman et al. (1968). An extension of the work Goodman et al. (1968) to the fully three-dimensional setting, together with a material model for cracks, was given in Ortiz & Pandolfi (1999). Within the cited paper, cracks were introduced between tetrahedral finite elements by successively releasing lateral element facets. In addition to their appealing simplicity, interface formulations show further beneficial features. For instance, they naturally lead to a continuous approximation of the considered crack's topology. Hence, tracking algorithms are not required (see Oliver et al. (2002)). Furthermore, complex

material failure involving crack branching, intersecting cracks and fragmentation is naturally covered, cf. Pandolfi & Ortiz (2002). The drawbacks of interface elements are the need for modifying the global data structure of the considered finite element code (such as the duplication of nodes) and the inherent mesh bias, i.e., the topology of the crack is spanned by the facets of the finite elements. The latter point is more serious and its elimination requires the application of adaptive strategies, cf. Gürses & Miehe (2009); Mosler (2007).

As an alternative to interface elements, discrete cracks can be embedded within finite elements, cf. Dvorkin et al. (1990). In this connection, two different approaches can be distinguished: nodal-based formulations and element-based techniques. While the extended finite element method Belytschko & Black (1999); Sukumar et al. (2000) and the phantom nodes approach Hansbo & Hansbo (2002); Jäger (2009) fall into the range of the first group, the so-called *embedded Strong Discontinuity Approach* (SDA), as introduced in Simo et al. (1993) in its modern form, belongs to the latter (see also Chaves (2003); Feist & Hofstetter (2007); Mosler & Meschke (2003); Sancho et al. (2007); Wells & Sluys (2001) for fully three-dimensional implementations). Comparative studies of the SDA and the XFEM were presented in Borja (2008); Jirásek (2000); Oliver et al. (2006b). Although nodal-based and element-based formulations are not equivalent, they share a lot of similarities. The probably most important of those is that they allow to approximate the topology of a crack (almost) independently of the underlying finite element discretization. Consequently, a pathological mesh bias is not observed. Furthermore, and focusing on element-based methods, the implementation of such finite element models is relatively straightforward and does not require any modification of the global data structure, cf. Mosler (2007); Wells & Sluys (2001). Unfortunately, the flexibility of embedded strong discontinuity approaches to allow a crack crossing finite elements arbitrarily necessitates the application of so-called *crack tracking algorithms*, cf. Areias & Belytschko (2005); Feist & Hofstetter (2007); Gasser & Holzzapfel (2006); Gravouil et al. (2002); Oliver et al. (2002). Such algorithms enforce continuity of the crack path. A comparison of some of these methods can be found in Jäger et al. (2008). Besides that their implementation is relatively time consuming, those methods show, at least, two more serious problems. First, they are often based on purely geometrical arguments, i.e., physics is sometimes missing. Second, they are based on the assumption that only one single crack is to be tracked. More precisely, intersecting cracks and crack branching are usually a priori excluded. Consequently, such processes cannot be modeled or require fundamental extensions of existing approaches.

A comparison of the features characterizing interface formulations and embedded crack models leads to the conclusion that a combination of such models combining their advantages would be desirable. That is precisely the idea proposed in the present paper. In line with Mosler (2005); Tano et al. (1998), an element-based embedded SDA is advocated. More precisely, in contrast to the original work Simo et al. (1993) and in line with interface elements, several discontinuities each of them being parallel to a facet of the considered finite element are introduced. By doing so, continuity of the crack path approximation is automatically fulfilled as within interface formulations and complex crack patterns showing crack branching, intersecting cracks or fragmentation can be easily simulated. However, the proposed finite element enrichment is purely local and thus, it is very efficient and can be implemented in a relatively straightforward fashion. Particularly, the global data structure is not affected. It is worth mentioning that the assumption of cracks being parallel to the facets of bulk finite elements leading to a certain mesh bias is not mandatory as within interface formulations. However, numerical benchmarks showed

that the resulting bias is not that pronounced.

Though the idea of multiple or intersecting embedded strong discontinuities is not entirely new, the existing prototype models Mosler (2005); Tano et al. (1998) are significantly extended in different directions within the present paper. In contrast to Mosler (2005); Tano et al. (1998) where two intersecting embedded strong discontinuities were analyzed in a two-dimensional setting for the first time by means of relatively simple academic benchmark problems with prescribed crack paths, a complete, fully three-dimensional finite element formulation is given in this paper. Particularly, the influence of different approximations of the displacement discontinuities and the number of cracks per element are carefully analyzed. Furthermore, a geometrically exact model, together with a thermodynamically sound finite strain constitutive law, is elaborated.

The remaining part of the paper is structured as follows: In Section 2, the kinematics of intersecting discontinuities is discussed, while Section 3 contains the constitutive models for the bulk material as well as that for material separation. The main part of the present paper is addressed in Section 4. There, the implementation of the novel intersecting embedded SDA is elaborated. Numerical examples demonstrating the performance of the resulting numerical formulation are finally discussed in Section 5.

2 Kinematics of discontinuous displacement fields

In this section, the kinematics induced by strong discontinuities is discussed. While Subsection 2.1 is associated with a single discontinuity, multiple displacement jumps are addressed in Subsection 2.2. Further details concerning the kinematical description of discontinuous deformation mappings can be found, e.g., in Oliver (1996); Simo et al. (1993).

2.1 Single strong discontinuity

In what follows, a body Ω occupying a closed domain in \mathbb{R}^3 is considered. If this body is subjected to sufficiently large externally applied loads, material failure will finally occur. In the present paper, focus is on localized failure in terms of cracking in quasi-brittle solids. Geometrically, cracks can be represented by an internal surface $\partial_s\Omega$ separating the body Ω into the two subbodies Ω^+ and Ω^- , see Fig. 1. Locally, the orientation of $\partial_s\Omega$ is defined by its normal vector \mathbf{N} .

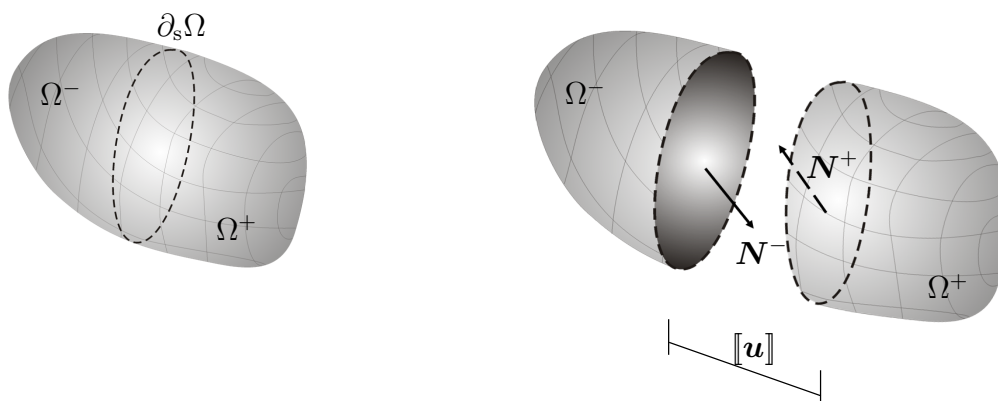


Figure 1: A body cut by a crack

As shown in Fig. 1, a displacement discontinuity (crack opening) between the two separated subbodies Ω^+ and Ω^- may form under subsequent loading. Based on the displacement fields in Ω^+ and Ω^- , this discontinuity can be computed as

$$[[\mathbf{u}]] := \mathbf{u}^+ - \mathbf{u}^- \quad (1)$$

with

$$\mathbf{u}^\pm = \lim_{\mathbf{X}^\pm \rightarrow \mathbf{P}} \mathbf{u}(\mathbf{X}^\pm) \quad \forall \mathbf{P} \in \partial_s \Omega. \quad (2)$$

Here, \mathbf{u}^+ and \mathbf{u}^- denote the right hand and the left hand limit of the displacement field at $\mathbf{P} \in \partial_s \Omega$.

Discontinuous displacement fields can be embedded into finite elements by means of different approaches such as the extended finite element method Belytschko & Black (1999); Sukumar et al. (2000), the phantom nodes method Hansbo & Hansbo (2002); Jäger (2009) or the *embedded Strong Discontinuity Approach* (SDA) Chaves (2003); Feist & Hofstetter (2007); Mosler & Meschke (2003); Sancho et al. (2007); Simo et al. (1993); Wells & Sluys (2001). In the present paper, the latter framework is utilized. Following Simo et al. (1993), the displacement field \mathbf{u} within the respective finite element is assumed to be of the type

$$\mathbf{u} = \bar{\mathbf{u}} + \hat{\mathbf{u}} = \bar{\mathbf{u}} + [[\mathbf{u}]] (H_s - \varphi), \quad (3)$$

where $\bar{\mathbf{u}}$ is a compatible, C^0 -continuous field, while the enhanced, incompatible part $\hat{\mathbf{u}}$ contains a displacement jump. According to Eq. (3), this enhancement is defined by the Heaviside function H_s and a smooth ramp function denoted as φ . φ is designed such that the enhanced, discontinuous part of the displacement field vanishes at the boundary of the considered finite element, i.e.,

$$[[\mathbf{u}]] (H_s - \varphi) = \mathbf{0} \quad \Rightarrow \quad \mathbf{u} = \bar{\mathbf{u}} \quad \forall \mathbf{X} \in \partial \Omega. \quad (4)$$

This allows to prescribe boundary conditions in terms of $\bar{\mathbf{u}}$. One choice complying with condition (4) is given by

$$\varphi = \sum_{i=1}^{\bar{\Omega}^+} N_i. \quad (5)$$

Here, N_i denote the standard interpolation function associated with node i . In Eq. (5), the sum has to be performed over all nodes belonging to the closure of Ω^+ , cf. Mosler (2004); Oliver (1996).

By applying the generalized derivative to the Heaviside function (cf. Stakgold (1998)),

$$\nabla H_s = \mathbf{N} \delta_s, \quad (6)$$

the deformation gradient is computed from Eq. (3) as

$$\mathbf{F} = \mathbf{1} + \nabla \bar{\mathbf{u}} + \nabla [[\mathbf{u}]] (H_s - \varphi) - [[\mathbf{u}]] \otimes \nabla \varphi + [[\mathbf{u}]] \otimes \mathbf{N} \delta_s. \quad (7)$$

In Eqs. (6) and (7), δ_s represents the Dirac-delta distribution and ∇ denotes the gradient operator with respect to the undeformed configuration ($\nabla(\bullet) = \partial(\bullet)/\partial \mathbf{X}$). Eq. (7) can be decomposed into a deformation gradient $\bar{\mathbf{F}}$ corresponding to the compatible and

continuous displacement field and an enhanced part \mathbf{H} resulting from the incompatible enhancement $\hat{\mathbf{u}}$, i.e.,

$$\mathbf{F} = \bar{\mathbf{F}} + \mathbf{H} \quad \text{with} \quad \begin{aligned} \bar{\mathbf{F}} &= \mathbf{1} + \nabla \bar{\mathbf{u}} \\ \mathbf{H} &= \nabla \llbracket \mathbf{u} \rrbracket (H_s - \varphi) - \llbracket \mathbf{u} \rrbracket \otimes \nabla \varphi + \llbracket \mathbf{u} \rrbracket \otimes \mathbf{N} \delta_s. \end{aligned} \quad (8)$$

Since $\hat{\mathbf{u}}$ is assumed as represented by an incompatible approximation, the displacement jump can be assumed as spatially constant ($\nabla \llbracket \mathbf{u} \rrbracket = \mathbf{0}$). Consequently,

$$\mathbf{F} = \mathbf{1} + \nabla \bar{\mathbf{u}} - \llbracket \mathbf{u} \rrbracket \otimes \nabla \varphi + \llbracket \mathbf{u} \rrbracket \otimes \mathbf{N} \delta_s. \quad (9)$$

Assumption $\nabla \llbracket \mathbf{u} \rrbracket = \mathbf{0}$ is common for most finite element formulations based on the embedded SDA, cf. Chaves (2003); Feist & Hofstetter (2007); Mosler & Meschke (2003); Sancho et al. (2007); Simo et al. (1993); Wells & Sluys (2001). The error resulting from this simplification is negligible, if the finite elements crossed by a crack are sufficiently small. However, assumption $\nabla \llbracket \mathbf{u} \rrbracket = \mathbf{0}$ is not mandatory, cf. Linder & Armero (2008).

2.2 Multiple, intersecting strong discontinuities

In contrast to the previous section, n possibly simultaneously active strong discontinuities per finite element are considered here. Consequently, a displacement field of the type

$$\mathbf{u} = \bar{\mathbf{u}} + \sum_{(i)=1}^n \llbracket \mathbf{u} \rrbracket^{(i)} (H_s^{(i)} - \varphi^{(i)}) \quad (i) = 1 \dots n. \quad (10)$$

is assumed. By applying the generalized derivative (6) to Eq. (10), together with $\nabla \llbracket \mathbf{u} \rrbracket^{(i)} = \mathbf{0}$, the deformation gradient is computed as

$$\mathbf{F} = \mathbf{1} + \nabla \bar{\mathbf{u}} - \sum_{(i)=1}^n \left[\llbracket \mathbf{u} \rrbracket^{(i)} \otimes \nabla \varphi^{(i)} \right] + \sum_{(i)=1}^n \left[\llbracket \mathbf{u} \rrbracket^{(i)} \otimes \mathbf{N}^{(i)} \delta_s^{(i)} \right]. \quad (11)$$

In Eqs. (10) and (11), $\llbracket \mathbf{u} \rrbracket^{(i)}$, $H_s^{(i)}$, $\varphi^{(i)}$, $\mathbf{N}^{(i)}$ and $\delta_s^{(i)}$ represent the displacement jump, the Heaviside function, the ramp function, the normal vector and the Dirac-delta distribution corresponding to discontinuity i , respectively.

Remark 1 *Interestingly and as already pointed out in Mosler (2005), the concept of multiple, intersecting strong discontinuities shows a strong analogy to so-called rotating crack formulations, cf. Mosler & Meschke (2003). More explicitly, by interpreting the sums in Eqs. (10) and (11) as the strain field induced by one equivalent resulting crack, the normal of that crack would rotate.*

3 Constitutive models

This section is concerned with material models. While in Subsection 3.1 a constitutive law for the bulk material is presented, a thermodynamically consistent cohesive model describing material separation is elaborated in Subsection 3.2.

3.1 Continuum material model

According to Section 2, the deformation gradient is regularly distributed in the bulk material ($\mathbf{X} \in \Omega^\pm$). Hence, standard continuum models can be applied. Here, a compressible Neo-Hookean material defined by a stored-energy function of the form

$$\Psi_{\text{reg}} = \lambda \frac{J^2 - 1}{4} - \left(\frac{\lambda}{2} + \mu \right) \ln J + \frac{\mu}{2} (\text{tr } \bar{\mathbf{C}} - 3) \quad (12)$$

is adopted. Clearly, other, more complicated constitutive models can be applied as well. In Eq. (12), λ and μ are Lamé constants, J denotes the determinant of the deformation gradient $\bar{\mathbf{F}}$ and $\bar{\mathbf{C}} = \bar{\mathbf{F}}^T \cdot \bar{\mathbf{F}}$ is the right Cauchy-Green tensor. Further details concerning the polyconvex stored-energy function Ψ_{reg} can be found in Ciarlet (1988). To complete the mechanical description of the bulk material, the first Piola-Kirchhoff stress tensor following from the standard Coleman & Noll procedure (cf. Coleman & Noll (1963)) is given as

$$\mathbf{P} = \partial_{\bar{\mathbf{F}}} \Psi_{\text{reg}} = \left(\lambda \frac{J^2 - 1}{2} - \mu \right) \mathbf{F}^{-T} + \mu \mathbf{F}. \quad (13)$$

3.2 Cohesive zone model

The cohesive zone concept in its modern form was introduced in Hillerborg et al. (1976), where the authors described failure of brittle materials by means of the so-called *fictitious crack model*. According to the cohesive zone concept, phenomena such as void nucleation and growth, micro-cracking, micro-scale yielding, interface leakage and other mechanisms leading to degradation of material, are condensed into a discrete plane (the crack). It is assumed that along this plane cohesive tractions, denoted by \mathbf{T}_s , resist to the separation of the bulk material. Cohesive tractions are constitutively defined by a cohesive (traction-separation) law and they are usually reciprocal to the crack width, as shown in Fig. 2.

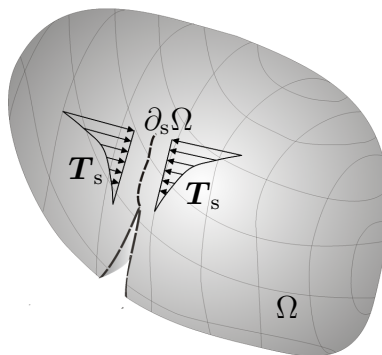


Figure 2: Modeling of material failure by means of a cohesive law

In this subsection, a cohesive law is derived in a thermodynamically consistent way. This is in sharp contrast to the most frequently applied approaches. Often, a traction-separation law of the type $\mathbf{T}_s = \mathbf{T}_s([\mathbf{u}])$ is directly postulated in an ad-hoc manner. It bears emphasis that such a model which does not derive from a potential can be interpreted as Cauchy-elastic. As a result, the restrictions imposed by the second law of

thermodynamics are usually not fulfilled, cf. Coleman & Noll (1963). In this connection, it should be noted that the existence of a potential is only a necessary condition for thermodynamical consistency, cf. Mosler & Scheider (2011). This can be seen by analyzing the models proposed in Needleman (1987); Ortiz & Pandolfi (1999); Park et al. (2009); Xu & Needleman (1993). Such models lead, at least, to three problems. First, since their underlying potentials include implicitly the Helmholtz as well as the dissipation, the dissipation cannot be computed – at least, not directly. Secondly and even more importantly, the aforementioned potentials have been designed for capturing the material response in case of loading. Therefore, an additional ad-hoc model completely independent of the one for loading is usually introduced for elastic unloading. Thus, loading and unloading are not defined jointly. Finally, models such as Needleman (1987); Ortiz & Pandolfi (1999); Park et al. (2009); Xu & Needleman (1993) are based on a decomposition of the traction vector into a normal component and a shear component. As pointed out in Mosler & Scheider (2011), they would require the introduction of additional membrane-type stresses for thermodynamical consistency at finite strains. However, such stresses have not been considered. This is probably the most important difference compared to the proposed model. The model advocated in the present section does not show the aforementioned problems and is thermodynamically consistent.

The thermodynamically consistent model presented here is based on an isotropic damage theory. Hereby, the scalar-valued variable $d \in [0, 1]$ indicates the degree of material degradation ($d = 0 \Leftrightarrow$ virgin material, $d = 1 \Leftrightarrow$ completely damaged material). With this damage variable, the Helmholtz energy Ψ_s of a not yet fully open crack is postulated to be of the type

$$\Psi_s = (1 - d) \Psi_0 \quad (14)$$

where Ψ_0 is the elastic stored energy functional. Clearly, $\Psi_0 = \Psi_0(\llbracket \mathbf{u} \rrbracket)$. However, Ψ_0 can indeed depend also on other variables defining a certain material anisotropy. For instance, the normal vector \mathbf{n} with respect to the deformed configuration is often included, i.e., $\Psi_0 = \Psi_0(\llbracket \mathbf{u} \rrbracket, \mathbf{n})$. This allows to differentiate between the normal and the shear mechanical response, see Ortiz & Pandolfi (1999). However, such a decomposition is not considered here. Consequently, it is assumed that $\Psi_0 = \Psi_0(\llbracket \mathbf{u} \rrbracket)$. Combing this with the condition of frame indifference leads to $\Psi_0 = \tilde{\Psi}_0(\|\llbracket \mathbf{u} \rrbracket\|)$. Hence, the elastic stored energy depends on the displacement discontinuity through its length. In the following, the simplest choice being possible is adopted, i.e.,

$$\Psi_0 = \frac{1}{2} E_s \|\llbracket \mathbf{u} \rrbracket\|^2. \quad (15)$$

Here, E_s is the initial stiffness of the interface. Evaluating the dissipation inequality for purely elastic unloading ($\mathcal{D}_s = 0$) gives rise to

$$\mathcal{D}_s = \mathbf{T}_s \cdot \dot{\llbracket \mathbf{u} \rrbracket} - \dot{\Psi}_s = \mathbf{T}_s \cdot \dot{\llbracket \mathbf{u} \rrbracket} - \frac{\partial \Psi_s}{\partial \llbracket \mathbf{u} \rrbracket} \cdot \dot{\llbracket \mathbf{u} \rrbracket} = 0, \quad \Rightarrow \quad \mathbf{T}_s = \frac{\partial \Psi_s}{\partial \llbracket \mathbf{u} \rrbracket} = (1-d) E_s \llbracket \mathbf{u} \rrbracket. \quad (16)$$

Accordingly, the traction vector predicted by the considered model is parallel to the displacement jump. This is a direct consequence of the isotropy of Ψ_0 . Inserting Eq. (16)₂ into the dissipation inequality yields its reduced form

$$\mathcal{D}_s = \mathbf{T}_s \cdot \dot{\llbracket \mathbf{u} \rrbracket} - \dot{\Psi}_s = Y \dot{d} \geq 0, \quad Y = -\frac{\partial \Psi_s}{\partial d}, \quad (17)$$

with the energy release rate Y . As evident from Ineq. (17), the second law of thermodynamics is automatically fulfilled, if d is monotonically increasing (no self-healing of

cracks). Ineq. (17) reveals further that d is thermodynamically conjugated to the energy release. Consequently, $d = d(Y)$. Furthermore, $Y = \Psi_0$ depends only on the displacement jump $[[\mathbf{u}]]$ (compare to Eq. (15)). As a result, duality arguments suggest $d = d([[\mathbf{u}]])$. In line with the elastic energy (15), it is assumed that $d = d([[\mathbf{u}]])$. However, since $[[\mathbf{u}]]$ can also decrease (crack closure), only the increase should affect damage accumulation. For that purpose, the internal variable κ is introduced and defined as

$$\dot{\kappa} = [[\dot{\mathbf{u}}]] \Rightarrow \kappa = \max \{ [[\mathbf{u}]]\}_{t_0}^t. \quad (18)$$

Thus, κ is postulated to be equal to the maximum reached equivalent displacement jump of the complete loading path (t denotes the pseudo time). The model is completed by a suitable evolution equation for the damage variable of the type $\dot{d} = d(\kappa)$ with $\dot{d} \geq 0$.

Remark 2 *Within the numerical simulations, the elastic stiffness E_s is computed as*

$$E_s = \frac{f_{tu}}{\kappa_0}. \quad (19)$$

Here, κ_0 is the initial value of κ and f_{tu} denotes the uniaxial tensile strength of the material. Clearly, the parameter E_s can be considered as a penalty stiffness. Therefore, κ_0 has to be chosen sufficiently small.

Remark 3 *Within the numerical simulations, the damage evolution is approximated by the function*

$$d = 1 - \frac{\kappa_0}{\kappa} \exp \left[- \frac{f_{tu} \kappa}{\mathcal{G}_f} \right] \quad (20)$$

with \mathcal{G}_f being the fracture energy. As evident from Eq. (20), d is monotonically increasing and thus, the second law of thermodynamics is fulfilled.

Remark 4 *If Newton's method is applied for solving the resulting discretized nonlinear boundary value problem, the linearization of the traction vector with respect to the displacement discontinuity is required. It is given by*

$$\frac{d\mathbf{T}_s}{d[[\mathbf{u}]]} =: \mathbf{C}_{[[\mathbf{u}]]} = (1 - d) E_s \mathbf{1} - H(\dot{\kappa}) \frac{E_s}{\kappa} \frac{\partial d}{\partial \kappa} [[\mathbf{u}]] \otimes [[\mathbf{u}]]. \quad (21)$$

In Eq. (21), H denotes the Heaviside function. Hence, only the first term is active in case of unloading ($\dot{\kappa} = 0$).

3.3 Coupling of material models: Condition of traction continuity

The material models for the bulk and the cohesive zone are till now completely separated. The coupling of them is provided by the condition of traction continuity, i.e.,

$$\mathbf{T}_s = \mathbf{T} \quad \text{with} \quad \mathbf{T} = \mathbf{T}^+ = -\mathbf{T}^-, \quad (22)$$

where \mathbf{T}^\pm denote the right and the left hand limit of the traction vector $\mathbf{T} = \mathbf{P} \cdot \mathbf{N}$. It bears emphasis that traction continuity implies equilibrium $[[\mathbf{T}]] = \mathbf{0}$ but not vice versa.

4 Numerical implementation

This section deals with the numerical implementation of finite elements with embedded strong discontinuities. The presented numerical formulation is based on the EAS concept, cf. Simo & Armero (1992); Simo & Rifai (1990). First, the governing system of equations is derived for a single finite element. Subsequently, locking effects of the resulting algorithmic model are analyzed in detail. To overcome them and to provide a robust and numerically efficient implementation, the standard SDA is modified. More precisely, the number of simultaneously active cracks within the respective finite element is increased yielding an intersecting SDA formulation. The final, novel finite element formulation combines the advantages of the SDA and those of interface elements.

4.1 Finite element formulation – Single displacement discontinuity

According to Oliver (1996); Simo et al. (1993), one possible implementation of the SDA is based on the EAS concept, cf. Simo & Rifai (1990). Such a numerical formulation is also presented in this subsection. Though this approach is not new for a single discontinuity, it represents the background for the novel intersecting SDA as discussed in Subsection 4.3. Furthermore, the fundamental notations are introduced in this section.

A straightforward transformation of the stationarity conditions given in Oliver (1996); Simo et al. (1993) to the finite strain regime yields

$$\int_{\Omega} \mathbf{P} : \nabla \bar{\boldsymbol{\eta}} \, dV - \int_{\Omega} \mathbf{B} \cdot \bar{\boldsymbol{\eta}} \, dV - \int_{\Gamma_{\mathbf{P}}} \mathbf{T}^* \cdot \bar{\boldsymbol{\eta}} \, dA = 0, \quad (23)$$

and

$$\int_{\Omega} \delta \mathbf{H} : \mathbf{P} \, dV = 0 \quad (24)$$

where $\bar{\boldsymbol{\eta}}$, \mathbf{B} , \mathbf{T}^* , $\delta \mathbf{H}$ and V denote a continuous test function, body forces, prescribed tractions at the Neumann boundary $\Gamma_{\mathbf{P}}$, the variation of the enhanced displacement gradient and the volume of the considered finite element, respectively. Clearly, the approximation of the complete boundary value problem requires a standard assembling procedure of the element contributions. Eq. (23) represents the principle of virtual works, while Eq. (24) states that the variation of the enhanced displacement gradient is orthogonal to the stress field. This equation is known as the L_2 -orthogonality condition, cf. Simo & Rifai (1990).

By choosing a certain Petrov-Galerkin approximation (see Oliver (1996); Simo et al. (1993)) for the variations of the enhanced gradient of the type

$$\delta \mathbf{H} = -\frac{1}{V} \boldsymbol{\beta} \otimes \mathbf{N} + \frac{1}{A_s} \boldsymbol{\beta} \otimes \mathbf{N} \delta_s, \quad (25)$$

the L_2 -orthogonality condition (24) reads

$$\frac{1}{V} \int_{\Omega} \mathbf{P} \cdot \mathbf{N} \, dV = \frac{1}{A_s} \int_{\partial_s \Omega} \mathbf{T}_s \, dA. \quad (26)$$

Here, $\boldsymbol{\beta} \in \mathbb{R}^3$ denotes the variation of the displacement jump and A_s is the area of the discontinuity. Accordingly, for the special choice (25), Eq. (24) is equivalent to the weak form of traction continuity. This is not the case for a standard Galerkin approximation,

cf. Mosler (2004); Simo & Oliver (1994). In summary, two equilibrium conditions are enforced within the SDA: global equilibrium as well as traction continuity.

In what follows, a finite element formulation is elaborated based on Eqs. (23) and (24). For that purpose, the continuous part $\bar{\mathbf{u}}$ of the displacement field \mathbf{u} and the continuous test function $\bar{\boldsymbol{\eta}}$ are approximated by using the standard shape functions N_i and the nodal values $\bar{\mathbf{u}}_i$ and $\bar{\boldsymbol{\eta}}_i$, i.e.,

$$\bar{\mathbf{u}} = \sum_i^{\text{nodes}} N_i \bar{\mathbf{u}}_i, \quad \bar{\boldsymbol{\eta}} = \sum_i^{\text{nodes}} N_i \bar{\boldsymbol{\eta}}_i \Rightarrow \nabla \bar{\mathbf{u}} = \sum_i^{\text{nodes}} \bar{\mathbf{u}}_i \otimes \nabla N_i, \quad \nabla \bar{\boldsymbol{\eta}} = \sum_i^{\text{nodes}} \bar{\boldsymbol{\eta}}_i \otimes \nabla N_i. \quad (27)$$

Inserting Eqs. (27) into the principle of virtual work (23), gives rise to the introduction of the nodal residuum

$$\mathbf{R}_{\bar{\mathbf{u}}}^i = \int_{\Omega} \mathbf{P} \cdot \nabla N_i \, dV - \int_{\Omega} N_i \mathbf{B} \, dV - \int_{\Gamma_{\mathbf{P}}} N_i \mathbf{T}^* \, dA. \quad (28)$$

In the following, all nodal vectors are summarized in the element residual $\mathbf{R}_{\bar{\mathbf{u}}}$ from which the respective global residuum can be computed by applying the standard assembling operation. Analogously, Eq. (26) is re-written into the residual form

$$\mathbf{R}_{\mathbf{s}} = -\frac{1}{V} \int_{\Omega} \mathbf{P} \cdot \mathbf{N} \, dV + \mathbf{T}_{\mathbf{s}} \quad (29)$$

where a spatially constant displacement jump has been assumed. The set of equations $\mathbf{R}_{\bar{\mathbf{u}}} = \mathbf{0}$ (the assembled counterpart) and $\mathbf{R}_{\mathbf{s}} = \mathbf{0}$ being nonlinear in $\bar{\mathbf{u}}$ and $[[\mathbf{u}]]$ are solved by employing Newton's method. This yields the linear set of equations

$$\begin{bmatrix} \mathbf{K}_{\bar{\mathbf{u}}\bar{\mathbf{u}}} & \mathbf{K}_{\bar{\mathbf{u}}\mathbf{s}} \\ \mathbf{K}_{\mathbf{s}\bar{\mathbf{u}}} & \mathbf{K}_{\mathbf{s}\mathbf{s}} \end{bmatrix}_{k-1} \begin{bmatrix} \Delta \bar{\mathbf{u}} \\ \Delta [[\mathbf{u}]] \end{bmatrix}_k = - \begin{bmatrix} \mathbf{R}_{\bar{\mathbf{u}}} \\ \mathbf{R}_{\mathbf{s}} \end{bmatrix}_{k-1}, \quad (30)$$

at the element level where the variables subscribed by $k-1$ are related to the previous iteration step. The stiffness matrices $\mathbf{K}_{\bar{\mathbf{u}}\bar{\mathbf{u}}}$, $\mathbf{K}_{\bar{\mathbf{u}}\mathbf{s}}$, $\mathbf{K}_{\mathbf{s}\bar{\mathbf{u}}}$ and $\mathbf{K}_{\mathbf{s}\mathbf{s}}$ are computed as

$$\mathbf{K}_{\bar{\mathbf{u}}\bar{\mathbf{u}}}^{ij} = \frac{\partial \mathbf{R}_{\bar{\mathbf{u}}}^i}{\partial \bar{\mathbf{u}}^j} = \int_{\Omega} \nabla N_i \overset{(2)}{\cdot} \frac{\partial \mathbf{P}}{\partial \mathbf{F}} \cdot \nabla N_j \, dV \quad (31)$$

$$\mathbf{K}_{\bar{\mathbf{u}}\mathbf{s}}^i = \frac{\partial \mathbf{R}_{\bar{\mathbf{u}}}^i}{\partial [[\mathbf{u}]]} = - \int_{\Omega} \nabla N_i \overset{(2)}{\cdot} \frac{\partial \mathbf{P}}{\partial \mathbf{F}} \cdot \nabla \varphi \, dV \quad (32)$$

$$\mathbf{K}_{\mathbf{s}\bar{\mathbf{u}}}^i = \frac{\partial \mathbf{R}_{\mathbf{s}}}{\partial \bar{\mathbf{u}}^i} = -\frac{1}{V} \int_{\Omega} \mathbf{N} \overset{(2)}{\cdot} \frac{\partial \mathbf{P}}{\partial \mathbf{F}} \cdot \nabla N_i \, dV \quad (33)$$

$$\mathbf{K}_{\mathbf{s}\mathbf{s}} = \frac{\partial \mathbf{R}_{\mathbf{s}}}{\partial [[\mathbf{u}]]} = \frac{1}{V} \int_{\Omega} \mathbf{N} \overset{(2)}{\cdot} \frac{\partial \mathbf{P}}{\partial \mathbf{F}} \cdot \nabla \varphi \, dV + \mathbf{C}_{[[\mathbf{u}]]}. \quad (34)$$

Here, the symbol $\overset{(2)}{\cdot}$ denotes the summation over the second index. The last term in (34) results from the linearization of the traction vector, cf. Eq. (21). Within the numerical implementation and in line with the original EAS concept proposed in Simo & Rifai (1990), the static condensation technique is utilized. Thereby, the maximum order of a matrix to be inverted is 3×3 .

Remark 5 According to the classifications given in Gasser & Holzapfel (2003); Jirásek (2000), the proposed formulation is referred to as *statically and kinematically optimal non-symmetric (SKON)*. It provides the correct transfer of the stresses between the cohesive zone and the bulk material. In addition, it satisfies the L_2 -orthogonality condition. From Eqs. (31) - (34) follows that the tangent stiffness matrix is symmetric only, if the vectors \mathbf{N} and $\nabla\varphi$ are parallel. Thus, the presented formulation leads to a computationally more expensive non-symmetric stiffness matrix in general. However, as noticed in Armero & Garikipati (1996), the underlying non-symmetric formulation captures highly localized deformations best. Moreover, the numerical stability and the convergence rate are much better for the SKON formulation compared to those of other implementations, cf. Oliver et al. (2006a).

4.2 Locking effects - A concise review

It is well known that a straightforward implementation of finite elements with a single embedded strong discontinuity can lead to locking effects, cf. Jirásek & Zimmermann (2001); Mosler (2004); Mosler & Meschke (2003). This can result in convergence problems, or in crack spreading. In the latter case, a macro-crack can be observed. However, a lot of surrounding micro-cracks are present as well. Hereby, the localization effect and material softening are underestimated, while the global dissipation is overestimated. Locking and spreading effects are visualized in Fig. 3 by means of an L-shaped frame.

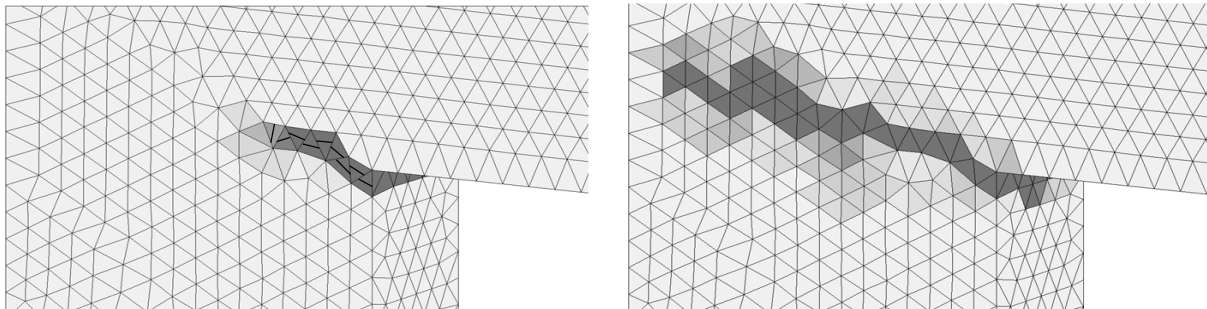


Figure 3: Locking and spreading effect: left: wrongly predicted crack normal in the highlighted element leads to stress locking and convergence problems; right: Although a macro-crack is formed, it is dispersed over a wider zone resulting in an underestimation of softening (overestimation of dissipation).

To overcome the aforementioned problems, different strategies have been developed. One possibility is to apply so-called *crack tracking algorithms*, which enforce crack path continuity, cf. Areias & Belytschko (2005); Feist & Hofstetter (2007); Gasser & Holzapfel (2006); Gravouil et al. (2002); Gürses & Miehe (2009); Mosler (2007); Oliver et al. (2002). A comparison of different approaches can be found in Jäger et al. (2008). Besides that their implementation is relatively time consuming, crack tracking algorithms show, at least, two more serious problems. First, they are often based on purely geometrical arguments, i.e., physics is sometimes missing. The only exception is the method proposed in Oliver et al. (2002) which is based on an analogy between a heat-like problem and the trajectories of the principal stresses. Second, they strongly rely on the assumption that only one single crack is to be tracked. Consequently, processes such as intersecting cracks or crack branching cannot be modeled or require fundamental extensions of existing approaches.

Alternative concepts avoiding the use of numerically expensive tracking algorithms can be also found in the literature. For instance, in Jirásek & Zimmermann (2001), the authors proposed the so-called *delayed embedded crack model* where the discontinuity is not introduced immediately after reaching the respective failure criterion. Instead, a smeared crack model is utilized first. After a certain threshold is reached, the transition from the smeared to the discrete model is enforced. In this way, the initial misprediction of the crack orientation can be eliminated.

Locking effects can also be reduced by applying the so-called *rotation crack model*, cf. Rots (1988). Here, a possible misprediction of the crack orientation is corrected by allowing the crack to rotate simultaneously according to the strains or stresses acting, see Cope et al. (1980); Mosler & Meschke (2003); Sancho et al. (2007); Tano et al. (1998). The efficiency of such approaches was demonstrated in Mosler & Meschke (2003). Clearly, since cracks can rotate in each finite element independently, this is an incompatible modeling technique leading to a discontinuous crack path. Furthermore, usually only one crack per element is considered in such formulations. Hence, processes characterized by intersecting cracks or crack branching are a priori excluded.

Summarizing the positive features of the approaches briefly sketched before, leads to a list of properties which should be fulfilled by a physically sound, desirable embedded SDA. This list reads:

- Continuous crack path approximation
- Multiple cracks within each finite element (intersecting cracks, branching)
- Strictly local formulation; no crack tracking algorithms.

A method which can fulfill all these points is the so-called *intersecting strong discontinuity approach* also known as *multiple crack approach*. Such a finite element formulation was briefly discussed in Jirásek & Zimmermann (2001); Tano et al. (1998). However, further details were not given. First computations can be found in Mosler (2005) where two orthogonal crack within each finite element have been considered. Besides the prototype implementations Jirásek & Zimmermann (2001); Mosler (2005); Tano et al. (1998) the *intersecting strong discontinuity approach* has not been addressed in a more detailed way yet. Therefore, it is further elaborated in the present paper.

4.3 Intersecting SDA

In Section 2.2, the displacement field and the deformation gradient have been given for several discontinuities per finite element. Following Subsection 3.3 (see also Eq. (29)), the discretized weak form of traction continuity reads now

$$\mathbf{R}_s^{(i)} = -\frac{1}{V} \int_{\Omega} \mathbf{P} \cdot \mathbf{N}^{(i)} \, dV + \mathbf{T}_s^{(i)} \quad (i) = 1 \dots n, \quad (35)$$

for each discontinuity. Again, the traction vector $\mathbf{T}_s^{(i)}$ follows from the constitutive law as discussed in Subsection 3.2, cf. Eq. (16)₂. In the following, only “self-softening” is considered, i.e., softening at cohesive plane i does not affect that of plane j . This assumption leads to an uncoupling of the internal variables, i.e.,

$$\kappa^{(i)} = \max(\kappa_{\text{tr}}^{(i)}, \| [\mathbf{u}]^{(i)} \|), \quad (36)$$

with $\kappa_{\text{tr}}^{(i)}$ being the value of $\kappa^{(i)}$ from the last converged step. Physically speaking, this uncoupling results in an anisotropic damage evolution.

Based on the principle of virtual work (28) and the weak form of traction continuity (35), a finite element formulation can be developed by means of the same discretization techniques as already introduced in Subsection 4.1. Utilizing a Newton's scheme, the linear set of equations

$$\begin{bmatrix} \mathbf{K}_{\bar{\mathbf{u}}\bar{\mathbf{u}}} & \mathbf{K}_{\bar{\mathbf{u}}\mathbf{s}}^{(1)} & \cdots & \mathbf{K}_{\bar{\mathbf{u}}\mathbf{s}}^{(n)} \\ \mathbf{K}_{\mathbf{s}\bar{\mathbf{u}}}^{(1)} & \mathbf{K}_{\mathbf{s}\mathbf{s}}^{(11)} & \cdots & \mathbf{K}_{\mathbf{s}\mathbf{s}}^{(1n)} \\ \vdots & & & \vdots \\ \mathbf{K}_{\mathbf{s}\bar{\mathbf{u}}}^{(n)} & \mathbf{K}_{\mathbf{s}\mathbf{s}}^{(n1)} & \cdots & \mathbf{K}_{\mathbf{s}\mathbf{s}}^{(nn)} \end{bmatrix}_{k-1} \begin{bmatrix} \Delta \bar{\mathbf{u}} \\ \Delta [\mathbf{u}]^{(1)} \\ \vdots \\ \Delta [\mathbf{u}]^{(n)} \end{bmatrix}_k = - \begin{bmatrix} \mathbf{R}_{\bar{\mathbf{u}}} \\ \mathbf{R}_{\mathbf{s}}^{(1)} \\ \vdots \\ \mathbf{R}_{\mathbf{s}}^{(n)} \end{bmatrix}_{k-1}. \quad (37)$$

has to be solved. The stiffness matrices occurring in Eq. (37) are defined as

$$\mathbf{K}_{\bar{\mathbf{u}}\bar{\mathbf{u}}}^{ij} = \frac{\partial \mathbf{R}_{\bar{\mathbf{u}}}^i}{\partial \bar{\mathbf{u}}^j}, \quad \mathbf{K}_{\bar{\mathbf{u}}\mathbf{s}}^{(i)} = \frac{\partial \mathbf{R}_{\bar{\mathbf{u}}}^i}{\partial [\mathbf{u}]^{(i)}}, \quad \mathbf{K}_{\mathbf{s}\bar{\mathbf{u}}}^{(i)} = \frac{\partial \mathbf{R}_{\mathbf{s}}^{(i)}}{\partial \bar{\mathbf{u}}}, \quad \mathbf{K}_{\mathbf{s}\mathbf{s}}^{(ij)} = \frac{\partial \mathbf{R}_{\mathbf{s}}^{(i)}}{\partial [\mathbf{u}]^{(j)}} \quad (j) = 1 \dots n. \quad (38)$$

Note that $\mathbf{C}_{[\mathbf{u}]}^{(ij)} = \mathbf{0}$, if $(i) \neq (j)$ (see Eq. (21)). This is a direct consequence of the assumed uncoupled softening evolution, i.e., $\kappa^{(i)} = \kappa^{(i)}([\mathbf{u}]^{(i)})$. For improving the numerical performance, a modified static condensation technique is proposed. More precisely, from the last line of Eq. (37), the increment of the displacement jump $\Delta [\mathbf{u}]_k^{(n)}$ is computed and inserted into the second-last line of Eq. (37). By doing so, the increment $\Delta [\mathbf{u}]_k^{(n-1)}$ can be calculated. This procedure can be successively repeated until the first line. As in the case of a single discontinuity per finite element, the maximum order of a matrix to be inverted remains 3×3 .

The stiffness matrix characterizing the intersecting SDA is non-symmetric in general. Clearly, efficiency would be further improved, if this matrix was symmetric. However, symmetry is only fulfilled, provided \mathbf{N} is parallel to the gradient of the ramp function φ , see Eq. (5). In this case, equation

$$\mathbf{N}^{(i)} = \frac{\nabla \varphi^{(i)}}{\|\nabla \varphi^{(i)}\|}. \quad (39)$$

holds. Eq. (39) implies that the discontinuities are parallel to the element facets, as shown in Fig. 4a. The respective failure mode is denoted as facet-mode in what follows. For edges, the ramp function $\varphi^{(i)}$ has to be replaced by the sum of the shape functions associated with the nodes defining the respective edge, cf. Fig. 4b. In this case, the failure mode is referred to as edge-mode. Consequently, such an assumption is equivalent to that of classical interface elements, cf. Ortiz & Pandolfi (1999); Pandolfi & Ortiz (2002). In both cases, the crack position and orientation are predefined by the respective triangulation. However, in contrast to classical interface elements, the implementation of the intersecting SDA is relatively straightforward (strictly local) and computationally more efficient. Similarly to classical interface elements, crack path continuity is automatically fulfilled, since the element facets are continuously connected in a finite element mesh. Thus, the proposed intersecting SDA combines the advantages of the standard SDA and those of classical interface elements.

Clearly, it should not be forgotten that the assumption of cracks being parallel to the facets or edges of finite elements leads to a certain mesh bias. However, since the SDA is strictly local, this effect is expected to be not strongly pronounced as in the case of interface finite elements. This will be confirmed by numerical benchmarks.

So far, it is not clear how many failure-modes and which of those (facet-mode or edge-mode) have to be considered. This question will be answered in the next section.

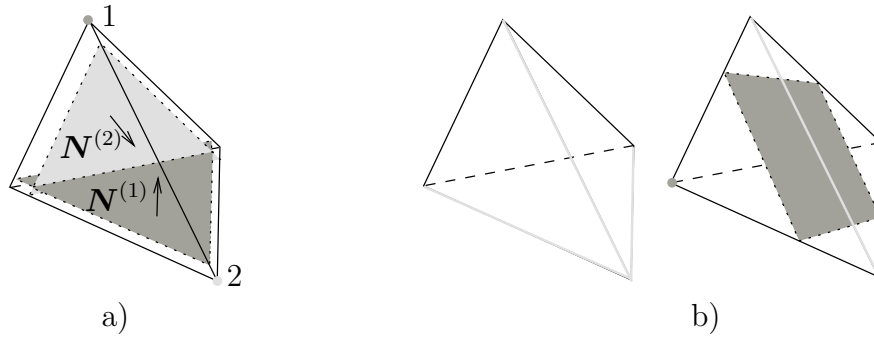


Figure 4: Intersecting SDA; a) two discontinuities parallel to the element facets. The corresponding marked nodes determine the ramp functions $\varphi^{(i)}$, see Eq. (39). b) additional failure modes parallel to the element edges and a discontinuity; the marked nodes determine the value of φ

Remark 6 Due to the partition of unity property of the standard shape functions, i.e.,

$$\sum_{i=1}^n N^{(i)} = 1 \quad (40)$$

not all failure modes have to be considered within the respective finite elements. More precisely, only three independent edge-modes are possible (see Fig. 4).

5 Numerical examples

In this section, the performance of the proposed intersecting SDA is investigated by means of two fully three-dimensional numerical examples: an L-shaped frame and bending of a notched beam.

5.1 L-shaped frame

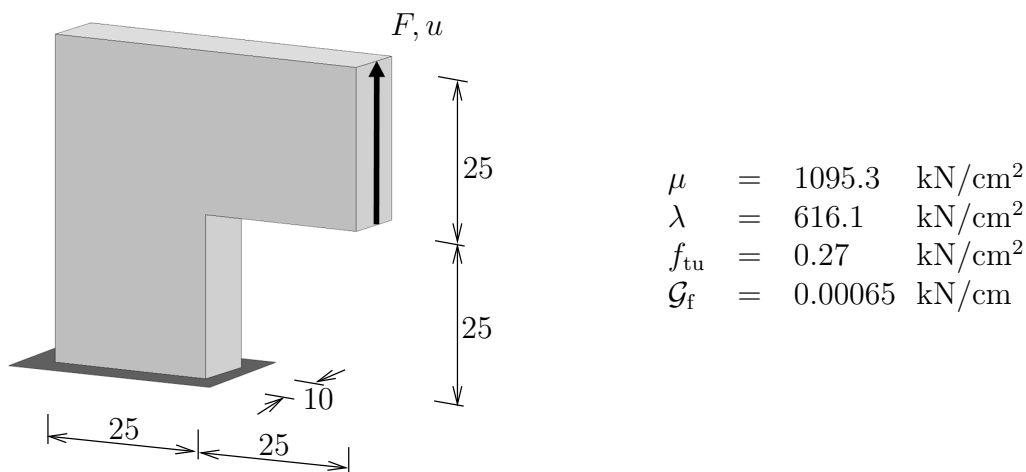


Figure 5: Numerical analysis of an L-shaped frame: dimensions [cm], boundary conditions and material parameters. The load is imposed by prescribing the vertical displacements at the highlighted surface (the respective horizontal displacements are not fixed).

This subsection deals with the numerical analysis of a concrete L-shaped frame. The geometry of the specimen, the material parameters and the boundary conditions are shown in Fig. 5. Experimental results of this setup were reported in Winkler et al. (2004). A corresponding three-dimensional numerical simulation can be found in Jäger et al. (2008) (see also Mosler (2002)). As mentioned in Mosler (2002); Winkler et al. (2004), cracking starts at the inner corner of the structure. Initially, this crack is slightly curved upwards. Under increasing load, the crack orientation changes and the crack propagates horizontally. Finally, the crack reaches the opposite facet of the frame and separates it into two parts.

To demonstrate the mesh independence of the proposed intersecting SDA formulation, three different discretizations are considered: one coarse mesh containing 6642 linear tetrahedral elements, and two finer triangulations consisting of 19928 and 33202 elements, respectively. For analyzing the effect of different numbers of cracks per element, the discontinuities are added successively. Initially, only one crack per element is taken into account. It is introduced parallel to the element's facet where the tensile stress reaches f_{tu} first. As shown in Figs. 6 and 7 (the enhanced elements are dark-colored), neither real softening nor localization can be observed in this case. More precisely, the enhanced elements are dispersed over the whole lower part of the specimen leading to an overestimation of the dissipation. With two cracks in each element, localization becomes visible. However, softening effects remain strongly underestimated. Not until three cracks, simultaneously allowed to be active, adequate localization and softening can be registered. The introduction of a fourth discontinuity does not further improve the results. Hence, this case is not considered in what follows.

A comparison of the crack paths predicted by the three discretizations is given in Fig. 8. Here, up to three discontinuities are allowed to be active in each finite element. The dark-colored elements are those enriched by a discontinuous displacement field. In Fig. 9, the load-displacement diagrams are compared to the experimental record. As evident from this figure, the results are independent of the spatial discretization and the softening behavior matches very well with the experimental observation. However, slight overestimations of the peak-load can be noted. The finest discretization leads to the stiffest material response. A reason for this might be the longest crack path (compared to other two discretizations), resulting in larger dissipation (the global dissipated energy is roughly proportional the crack length), cf. Mosler (2002). The numerically computed crack path corresponding to the finest discretization is compared to experimental observations in Fig. 10. Accordingly, an excellent agreement is obvious.

Remark 7 *The L-shaped frame was re-analyzed by considering also discontinuities being parallel to the element edges. The underlying idea of this modification is that the orientation of newly introduced cracks may better match to the directions of the maximum tensile stress. However, this modification did not improve the results, while only increasing the numerical costs. Therefore, this extension will not be applied in the remaining part of the paper.*

Remark 8 *As already mentioned, the intersecting SDA is based on an anisotropic evolution of softening. More precisely, the internal variables $\kappa^{(i)}$ associated with each element facet may differ from each other. As a consequence, the total fracture energy is greater than that related to a single crack concept. Although the adopted model is more realistic, an isotropic character of the damage model can be enforced by assigning the same internal variable to all discontinuities within the respective finite element. However, numerical*

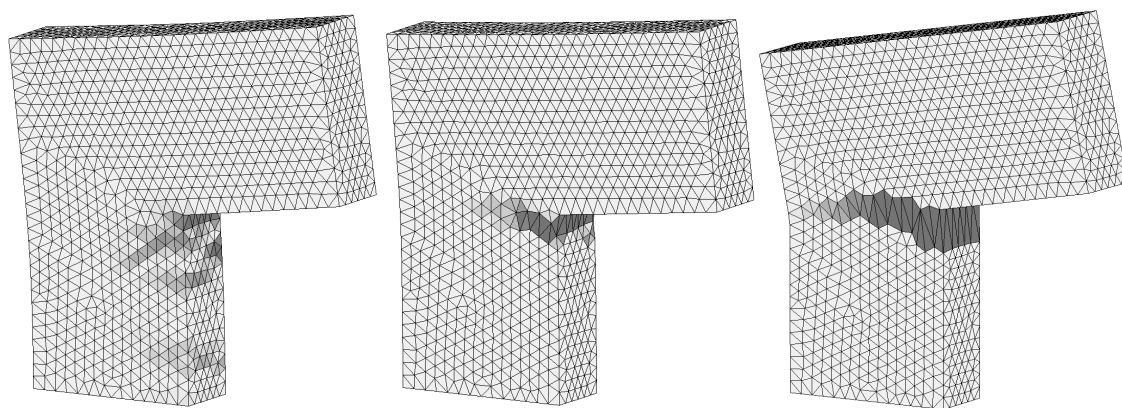


Figure 6: Numerical analysis of an L-shaped frame: comparison of crack paths for one, two and three (four) discontinuities per element. 100-fold magnification of the displacements

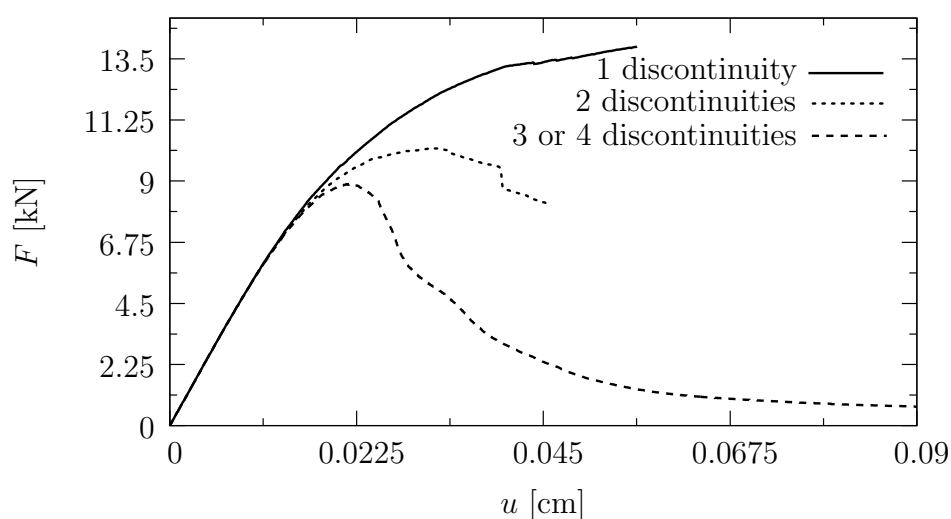


Figure 7: Numerical analysis of an L-shaped frame: comparison of load-displacement diagrams for one, two and three (four) discontinuities per element

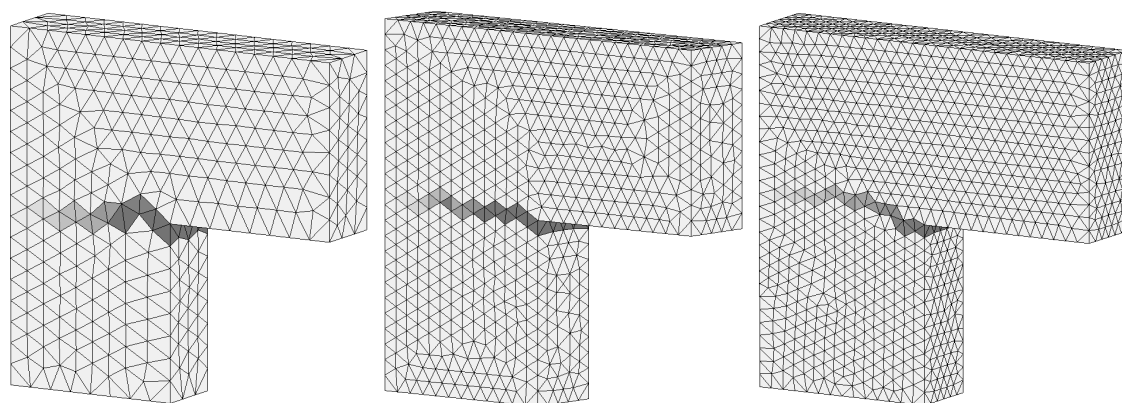


Figure 8: Numerical analysis of an L-shaped frame: crack paths for three different discretizations. Up to three discontinuities are active in each of the enhanced finite elements (final stage of deformation, $u = 0.09$ cm)

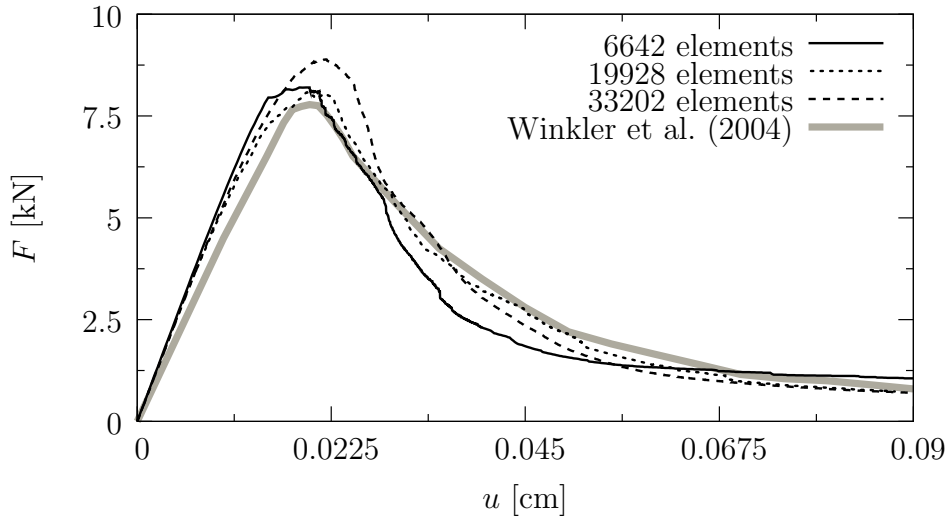


Figure 9: Numerical analysis of an L-shaped frame: load-displacement diagrams for the three different discretizations compared to experimental results

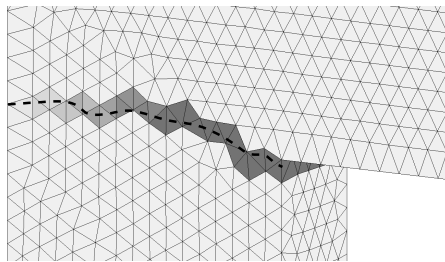


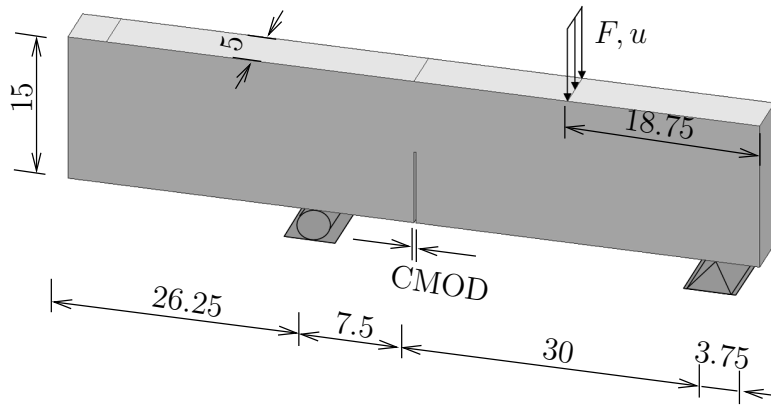
Figure 10: Numerical analysis of an L-shaped frame: comparison of the numerically predicted crack path to experimental results, cf. Winkler et al. (2004) (dashed line)

simulations showed that both assumptions (independent $\kappa^{(i)}$, or only one κ) lead to almost the same results for the analyzed structure.

Remark 9 *The material response of each discontinuity is modeled by the constitutive law as described in Subsection 3.2. This interface law is based on an isotropic damage model. As a result, the fracture energies in mode-I and mode-II or mode-III are implicitly assumed to be identical. Although this is a frequently made assumption, it is not very realistic for brittle materials in general. For this reason, two justifications for the chosen model are given here. First, the presented numerical framework can be applied to almost every traction-separation law. Therefore, the considered model represents just an admissible thermodynamically consistent choice. Secondly and equally importantly, a decomposition of the model into different failure modes, requires a decomposition of the traction vector and the displacement jump into normal and shear components. In the case of a geometrically exact and thermodynamically consistent description, many questions are still open and controversially discussed for such models, cf., e.g., Mergheim & Steinmann (2006).*

5.2 Bending of a notched beam

The present example is taken from Gálvez et al. (1998), where the authors documented a number of mixed mode failure experiments on notched beams. The geometry, the material properties and the boundary conditions are shown in Fig. 11. The width of the notch is 0,2 cm. The relative displacement between two notch points at the bottom side along the beam axis is defined as CMOD (crack mouth opening displacement). A three-dimensional numerical analysis of the same specimen by applying the XFEM can be found in Areias & Belytschko (2005), while a crack path prediction by using classical interface elements is presented in Gürses & Miehe (2009).



$$\begin{aligned}
 \mu &= 1610.17 \text{ kN/cm}^2 \\
 \lambda &= 905.72 \text{ kN/cm}^2 \\
 f_{tu} &= 0.3 \text{ kN/cm}^2 \\
 \mathcal{G}_f &= 0.00069 \text{ kN/cm}
 \end{aligned}$$

Figure 11: Numerical analysis of a notched beam: dimensions [cm], boundary conditions and material parameters

Four different finite element discretizations are considered. Two of them are uniformly distributed, containing 11077 and 31356 linear tetrahedral elements, respectively. Another two discretizations are refined in the region where the crack path is expected to propagate, while they are relatively coarse in the remaining part of the specimen. These two meshes consist of 13008 and 21295 elements, respectively. As in the previous example, up to three discontinuities in each finite element are introduced.

The computed crack paths associated with the different discretizations are visualized in Fig. 12. The enhanced elements are dark-colored. For all triangulations a crack propagates from the notch toward the upper surface of the beam, building approximately an angle of 30° with respect to the vertical direction at the initial crack tip. This is in excellent agreement with experimental and numerical predictions, cf. Gálvez et al. (1998) and Gürses & Miehe (2009). The load-CMOD curves are given in Fig. 13. Again, only a minor mesh-dependence is observed. Despite the differences in the peak-load, the numerically computed results match the experimental record well. It should be noted that the material parameters have been chosen according to Gálvez et al. (1998). An additional fine tuning was not performed.

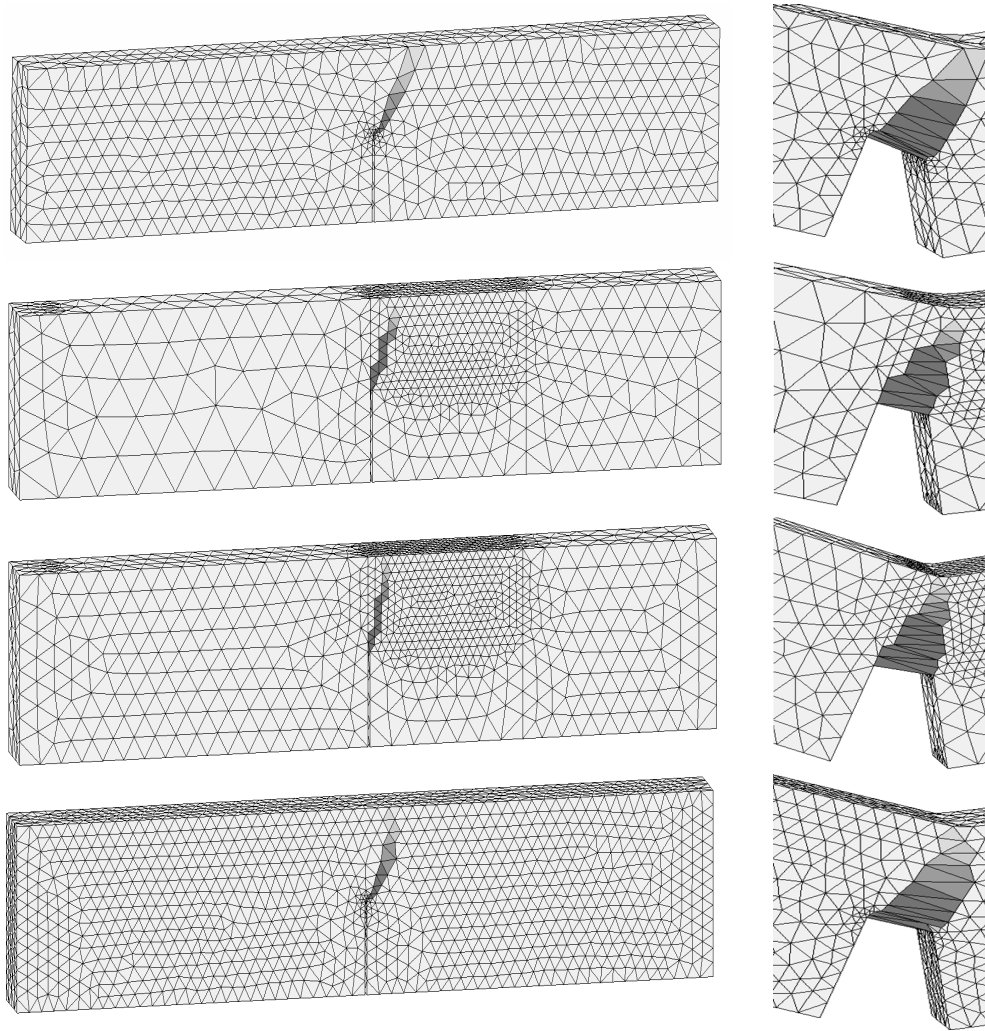


Figure 12: Numerical analysis of a notched beam: four different discretizations; left: crack path predictions, right: displacements magnified by a factor of 200 (final stage of deformation)

6 Concluding remarks

An efficient numerical framework suitable for three-dimensional analyses of quasi-brittle material failure has been elaborated in the present paper. By comparing the features of different discrete crack approaches such as interface formulations and embedded crack models, the conclusion was drawn that a novel scheme combining all advantages would be desirable. For this reason, a standard embedded Strong Discontinuity Approach (SDA) was extended. More precisely and in line with classical interface elements, several discontinuities each of them being parallel to a facet or an edge of the considered finite element were introduced. By doing so, continuity of the crack path approximation is automatically fulfilled as within interface formulations and complex crack patterns showing crack branching, intersecting cracks or fragmentation can be easily simulated. However and in contrast to standard interface elements, the proposed finite element enrichment is purely local and thus, it is very efficient and can be implemented in a relatively straightforward fashion. For instance, the static condensation technique can be applied and the resulting tangent stiffness matrix is symmetric (for associative material models). Furthermore and

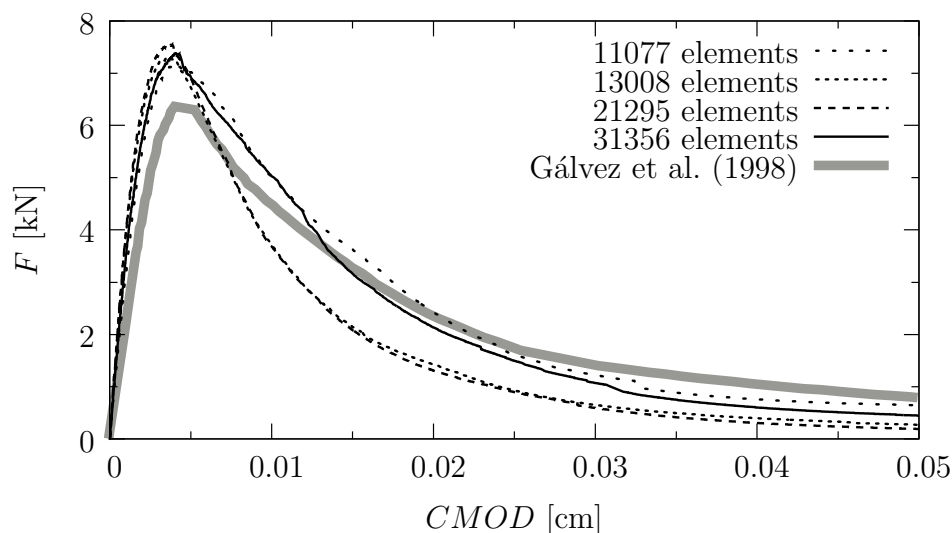


Figure 13: Numerical analysis of a notched beam: computed load-CMOD diagrams compared to experimental results

equally important, the global data structure is not affected. As a constitutive prototype model, a thermodynamically consistent, large strain, isotropic damage models was elaborated and implemented. However, it bears emphasis that the novel finite element formulation is not restricted to any specific constitutive law. It was shown that several simultaneously active discontinuities in each finite element are required to capture highly localized material failure. The performance and predictive ability of the model were demonstrated by means of two benchmark examples. These examples showed that the inherent mesh bias (cracks are parallel to facets or edges of finite elements) is not that pronounced.

References

- AREIAS, P. & BELYTSCHKO, T. (2005): *Analysis of three-dimensional crack initiation and propagation using the extended finite element method*, in: International Journal of Numerical Methods in Engineering, Volume 63, 760–788.
- ARMERO, F. & GARIKIPATI, K. (1996): *An analysis of strong discontinuities in multiplicative finite strain plasticity and their relation with the numerical simulation of strain localization in solids*, in: International Journal for Solids and Structures, Volume 33, 2863–2885.
- BARENBLATT, G. (1962): *The mathematical theory of equilibrium cracks in brittle fracture*, in: Advances in Applied Mechanics, Volume 7, 55–129.
- BELYTSCHKO, T. & BLACK, T. (1999): *Elastic crack growth in finite elements with minimal remeshing*, in: International Journal of Numerical Methods in Engineering, Volume 45, 601–620.
- BORJA, R. (2008): *Assumed enhanced strain and the extended finite element methods: A unification of concepts*, in: Computer Methods in Applied Mechanics and Engineering, Volume 197, 2789–2803.

- CHAVES, E. (2003): *A Three Dimensional Setting for Strong Discontinuities Modelling in Failure Mechanics* 2003, Dissertation, UPC Barcelona.
- CIARLET, P. (1988): *Mathematical Elasticity, Volume 1: Three-Dimensional Elasticity*, North-Holland, Amsterdam 1988.
- COLEMAN, B. & NOLL, W. (1963): *The thermodynamics of elastic materials with heat conduction and viscosity*, in: *Archive for Rational Mechanics and Analysis*, Volume 13, 167–178.
- COPE, R., RAO, P., CLARK, L. & NORRIS, P. (1980): *Modelling of reinforced concrete behaviour for finite element analysis of bridge slabs*, in: *Numerical Methods for Nonlinear Problems*, Pineridge Press, Swansea 1980, pp. 457–470.
- DE BORST, R. (2001): *Non-linear analysis of frictional materials* 2001, Dissertation, Delft University of Technology.
- DUGDALE, D. (1960): *Yielding of steel sheets containing slits*, in: *Journal of the Mechanics and Physics of Solids*, Volume 8, 100–108.
- DVORKIN, E., CUITINO, A. & GIOIA, G. (1990): *Finite elements with displacement interpolated embedded localization lines insensitive to mesh size and distortions*, in: *International Journal of Numerical Methods in Engineering*, Volume 30, 541–564.
- FEIST, C. & HOFSTETTER, G. (2007): *Three-dimensional fracture simulations based on the SDA*, in: *International Journal of Numerical and Analytical Methods in Geomechanics*, Volume 31, 189–212.
- GÁLVEZ, J., ELICES, M., GUINEA, G. & PLANAS, J. (1998): *Mixed Mode Fracture of Concrete under Proportional and Nonproportional Loading*, in: *International Journal of Fracture*, Volume 94, 267–284.
- GASSER, T. & HOLZAPFEL, G. (2003): *Geometrically non-linear and consistently linearized embedded strong discontinuity models for 3D problems with an application to the dissection analysis of soft biological tissues*, in: *Computer Methods in Applied Mechanics and Engineering*, Volume 192, 5059–5098.
- GASSER, T. & HOLZAPFEL, G. (2006): *3D Crack propagation in unreinforced concrete. A two-step algorithm for tracking 3D crack paths*, in: *Computer Methods in Applied Mechanics and Engineering*, Volume 195, 5198–5219.
- GOODMAN, R., TAYLOR, R. & BREKKE, T. (1968): *A model for the mechanics of jointed rock.*, in: *Journal of the Soil Mechanics and Foundations Division ASCE*, Volume 94(SM3), 637–659.
- GRAVOUIL, A., MOËS, N. & BELYTSCHKO, T. (2002): *Non-planar 3D crack growth by the extended finite element and level sets - Part II: Level set update*, in: *International Journal of Numerical Methods in Engineering*, Volume 53, 2569–2586.
- GÜRSES, E. & MIEHE, C. (2009): *A computational framework of three-dimensional configurational-force-driven brittle crack propagation*, in: *Computer Methods in Applied Mechanics and Engineering*, Volume 198, 1413–1428.

- HANSBO, A. & HANSBO, P. (2002): *An unfitted finite element method, based on Nitsche's method, for elliptic interface problems*, in: Computer Methods in Applied Mechanics and Engineering, Volume 191, 5537–5552.
- HILLERBORG, A., MODEER, M. & PETERSSEN, P. (1976): *Analysis of crack formation and crack growth in concrete by means of fracture mechanics and finite elements*, in: Cement and Concrete Research, Volume 6, 773–782.
- JÄGER, P. (2009): *Theory and numerics of three-dimensional strong discontinuities at finite strains* 2009, Dissertation, University of Kaiserslautern.
- JÄGER, P., STEINMANN, P. & KUHL, E. (2008): *Modeling three-dimensional crack propagation - A comparison of crack path tracking strategies*, in: International Journal of Numerical Methods in Engineering, Volume 76, 1328–1352.
- JIRÁSEK, M. (2000): *Comparative study on finite elements with embedded discontinuities*, in: Computer Methods in Applied Mechanics and Engineering, Volume 188, 307–330.
- JIRÁSEK, M. & ZIMMERMANN, T. (2001): *Embedded crack model: Part I. Basic formulation. Part II: Combination with smeared cracks*, in: International Journal of Numerical Methods in Engineering, Volume 50, 1269–1305.
- LINDER, C. & ARMERO, F. (2008): *New finite elements with embedded strong discontinuities for finite deformations*, in: Computer Methods in Applied Mechanics and Engineering, Volume 197, 3138–3170.
- MERGHEIM, J. & STEINMANN, P. (2006): *A geometrically nonlinear FE approach for the simulation of strong and weak discontinuities*, in: Computer Methods in Applied Mechanics and Engineering, Volume 195, 37–42, 5037–5052.
- MOSLER, J. (2002): *Finite Elemente mit sprungstetigen Abbildungen des Verschiebungsfeldes für numerische Analysen lokalisierter Versagenszustände in Tragwerken* 2002, Dissertation, Ruhr University Bochum.
- MOSLER, J. (2004): *On the Modeling of Highly Localized Deformations Induced by Material Failure: The Strong Discontinuity Approach*, in: Archives of Computational Methods in Engineering, Volume 11, 389–446.
- MOSLER, J. (2005): *On advanced solution strategies to overcome locking effects in strong discontinuity approaches*, in: International Journal of Numerical Methods in Engineering, Volume 63, 1313–1341.
- MOSLER, J. (2007): *On the numerical modeling of localized material failure at finite strains by means of variational mesh adaption and cohesive elements* 2007, Habilitation, Ruhr University Bochum.
- MOSLER, J. & MESCHKE, G. (2003): *3D modelling of strong discontinuities in elastoplastic solids: fixed and rotating localization formulations*, in: International Journal of Numerical Methods in Engineering, Volume 57, 1553–1576.
- MOSLER, J. & SCHEIDER, I. (2011): *A thermodynamically and variationally consistent class of damage-type cohesive models*, in: Journal of the Mechanics and Physics of Solids, Submitted.

- NEEDLEMAN, A. (1987): *A continuum model for void nucleation by inclusion debonding*, in: *Journal of Applied Mechanics – Transactions of the ASCME*, Volume 54, 525–531.
- NEEDLEMAN, A. (1990): *An analysis of decohesion along an imperfect interface*, in: *International Journal of Fracture*, Volume 42, 21–40.
- OLIVER, J. (1996): *Modelling strong discontinuities in solid mechanics via strain softening constitutive equations. Part 1: Fundamentals. Part 2: Numerical simulation*, in: *International Journal of Numerical Methods in Engineering*, Volume 39, 3575–3623.
- OLIVER, J., HUESPE, A., BLANCO, S. & LINERO, D. (2006a): *Stability and robustness issues in numerical modeling of material failure with the strong discontinuity approach*, in: *Computer Methods in Applied Mechanics and Engineering*, Volume 195, 7093–7114.
- OLIVER, J., HUESPE, A., SAMANIEGO, E. & CHAVES, E. (2002): *On strategies for tracking strong discontinuities in computational failure mechanics*, in: *Proceedings of Fifth World Congress on Computational Mechanics (WCCM V)*, Vienna University of Technology, Austria 2002.
- OLIVER, J., HUESPE, A. & SANCHES, P. (2006b): *A comparative study on finite elements for capturing strong discontinuities: E-FEM vs. X-FEM*, in: *Computer Methods in Applied Mechanics and Engineering*, Volume 195, 4732–4752.
- ORTIZ, M. & PANDOLFI, A. (1999): *Finite-deformation irreversible cohesive elements for three-dimensional crack-propagation analysis*, in: *International Journal of Numerical Methods in Engineering*, Volume 44, 1267–1282.
- PANDOLFI, A. & ORTIZ, M. (2002): *An Efficient Adaptive Procedure for Three-Dimensional Fragmentation Simulation*, in: *Engineering with Computers*, Volume 18, 148–159.
- PARK, K., PAULINO, G. & ROESLER, J. (2009): *A unified potential-based cohesive model of mixed-mode fracture*, in: *Journal of the Mechanics and Physics of Solids*, Volume 57, 891–908.
- PEERLINGS, R., DE BORST, R., BREKELMANS, W. & DE VREE, J. (1998): *Gradient enhanced damage for quasi-brittle materials*, in: *International Journal of Numerical Methods in Engineering*, Volume 39, 3391–3403.
- PIJAUDIER-CABOT, G. & BAŽANT, Z. (1987): *Nonlocal damage theory*, in: *Journal of Engineering Mechanics (ASCE)*, Volume 113, 1512–1533.
- ROTS, J. (1988): *Computational modeling of concrete fracture 1988*, Dissertation, Delft University of Technology.
- SANCHO, J., PLANAS, J., FATHY, A., GÁLVEZ, J. & CENDÓN, D. (2007): *Three-dimensional simulation of concrete fracture using embedded crack elements without enforcing crack path continuity*, in: *International Journal of Numerical and Analytical Methods in Geomechanics*, Volume 31, 173–187.
- SIMO, J. & ARMERO, F. (1992): *Geometrically non-linear enhanced strain mixed methods and the method of incompatible modes*, in: *International Journal of Numerical Methods in Engineering*, Volume 33, 1413–1449.

- SIMO, J. & OLIVER, J. (1994): *A new approach to the analysis and simulation of strain softening in solids*, in: BAŽANT, Z., BITTNER, Z., JIRÁSEK, M. & MAZARS, J. (Eds.): *Fracture and Damage in Quasibrittle Structures*, E. & F.N. Spon, London 1994, pp. 25–39.
- SIMO, J., OLIVER, J. & ARMERO, F. (1993): *An analysis of strong discontinuities induced by strain-softening in rate-independent inelastic models*, in: *Computational Mechanics*, Volume 12, 277–296.
- SIMO, J. & RIFAI, M. (1990): *A class of mixed assumed strain methods and the method of incompatible modes*, in: *International Journal of Numerical Methods in Engineering*, Volume 29, 1595–1638.
- STAKGOLD, I. (1998): *Green's functions and boundary value problems*, Wiley 1998.
- SUKUMAR, N., MOËS, N., MORAN, B. & BELYTSCHKO, T. (2000): *Extended finite element method for three-dimensional crack modelling*, in: *International Journal of Numerical Methods in Engineering*, Volume 48, 1549–1570.
- TANO, R., KLISINSKI, M. & OLOFSSON, T. (1998): *Stress locking in the inner softening band method: A study of the origin and how to reduce the effects.*, in: DE BORST, R., BIĆANIĆ, N., MANG, H. & MESCHKE, G. (Eds.): *Computational Modeling of Concrete Structures*, Balkema, Rotterdam 1998, pp. 329–335.
- WELLS, G. & SLUYS, L. (2001): *Three-dimensional embedded discontinuity model for brittle fracture*, in: *International Journal for Solids and Structures*, Volume 38, 897–913.
- WINKLER, B., HOFSTETTER, G. & LEHAR, H. (2004): *Application of a constitutive model for concrete to the analysis of a precast segmental tunnel lining*, in: *International Journal of Numerical and Analytical Methods in Geomechanics*, Volume 28, 797–819.
- XU, X. & NEEDLEMAN, A. (1993): *Void nucleation by inclusion debonding in a crystal matrix*, in: *Modelling and Simulation in Materials Science and Engineering*, Volume 1, 111–132.

Nomenclature

| | |
|--------------------------------------|---|
| A_s | Area of the surface showing strong discontinuities |
| \mathbf{N} | Normal vector to the discontinuity (reference configuration) |
| V | Volume of a finite element |
| dA, dV | Differential area and volume element |
| $\mathbf{u}, [\mathbf{u}]$ | Displacement field and displacement jump |
| $\bar{\mathbf{u}}, \hat{\mathbf{u}}$ | Continuous and discontinuous part of the displacement field |
| \mathbf{F} | Deformation gradient |
| $\bar{\mathbf{F}}, \mathbf{H}$ | Continuous and enhanced part of \mathbf{F} |
| J | Jacobian of the deformation gradient |
| \mathbf{C} | Right Cauchy–Green tensor |
| H_s | Heaviside function |
| δ_s | Dirac-delta distribution |
| φ | Ramp function for designing the discontinuous displacement field |
| N_i | Shape function of node i |
| \mathcal{D}_s | Dissipation at the surface showing strong discontinuities |
| Y | Thermodynamic force conjugated to the internal variable κ |
| d | Scalar-valued damage variable |
| κ | Maximum reached equivalent displacement jump |
| Ψ_{reg} | Helmholtz energy related to the bulk material |
| Ψ_s | Helmholtz energy related to material separation |
| f_{tu} | Uniaxial tensile strength |
| \mathcal{G}_f | Fracture energy (related to mode-I fracture) |
| λ, μ | Lamè constants |
| \mathbf{P} | First Piola-Kirchhoff stress tensor |
| \mathbf{T} | Piola traction vector |
| \mathbf{T}_s | Cohesive traction vector |
| $\mathbf{C}_{[\mathbf{u}]}$ | Tangent stiffness tensors of the cohesive zone, i.e., $d\mathbf{T}_s = \mathbf{C}_{[\mathbf{u}]} \cdot d[\mathbf{u}]$ |
| \mathbf{T}^* | Prescribed tractions (Neumann boundary) |
| \mathbf{B} | Body forces |
| $\bar{\eta}, \beta$ | Continuous and discontinuous test function (virtual work) |
| \mathbf{K} | Stiffness matrix |
| \mathbf{R} | Residual vector |
| $\mathbf{1}$ | Second-order identity tensor |
